Cryo-ET of HIV reveals Env positioning on Gag lattice and structural variation among Env trimers

Vidya Mangala Prasad[1], Daniel P. Leaman[4], Klaus N. Lovendahl[1], Mark A. Benhaim[1]†, Edgar A. Hodge[1], Michael B. Zwick[4] and Kelly K. Lee[1,2,3*]

1. Department of Medicinal Chemistry, University of Washington, Seattle, WA 98195, USA.
2. Biological Physics, Structure and Design Graduate Program, University of Washington, Seattle, WA 98195, USA.
3. Department of Microbiology, University of Washington, Seattle, WA 98195, USA.
4. Department of Immunology and Microbiology, The Scripps Research Institute, La Jolla, CA 92037, USA

*Correspondence to: kklee@uw.edu

†Current Address: Alkermes, Inc., 900 Winter St, Waltham, MA 02451, USA.

Summary:

HIV-1 Env mediates viral entry into host cells and is the sole target for neutralizing antibodies. However, Env structure and organization in its native virion context has eluded detailed characterization. Here we used cryo-electron tomography to analyze Env in mature and immature HIV-1 particles. Immature particles showed distinct Env positioning relative to the underlying Gag lattice, providing insights into long-standing questions about Env incorporation. A 9.1Å sub-tomogram averaged reconstruction of virion-bound Env in conjunction with structural mass spectrometry revealed unexpected features, including a variable central core of the gp41 subunit,

heterogeneous glycosylation between protomers plus a flexible stalk that allows Env tilting and variable exposure of neutralizing epitopes. Together, our results provide an integrative understanding of HIV assembly and structural variation in Env antigen presentation.

Keywords: HIV Env glycoprotein, HIV assembly, Gag-Env interaction, Cryo-electron tomography, sub-tomogram averaging, structural mass spectroscopy.

Introduction:

Human Immunodeficiency Virus-1 (HIV-1) continues to infect nearly two million people worldwide each year, with no available vaccine against the virus (Pandey and Galvani 2019). The envelope glycoprotein (Env) on the surface of HIV-1 is an essential viral entry machine that mediates binding to host cell receptors and subsequent membrane fusion. As the sole target for neutralizing antibodies, Env is also of singular importance for vaccine design efforts (van Gils and Sanders 2013). Env is translated as a precursor gp160 protein, which trimerizes, and is cleaved into gp120 and gp41 subunits that are primarily responsible for receptor binding and fusion, respectively. The gp120 and gp41 subunits remain as non-covalently associated heterodimers with gp41 embedded in the viral membrane via its transmembrane domain (TMD) and the C-terminal cytoplasmic domain (CTD) in the viral lumen. On incorporation into budding virions, Env CTD interacts with the matrix domain (MA) of immature Gag polyprotein which assembles as a membrane-associated lattice on the inner side of the viral bilayer (Checkley, Luttge et al. 2011, Tedbury and Freed 2014).

Recent insights into Env structure have primarily come from studies of engineered, truncated forms of the trimer ectodomain (such as SOSIPs) (Ward and Wilson 2015, Stewart-

47 Jones, Soto et al. 2016), while details of Env structure in its viral membrane context, including its
48 organization relative to other viral components, has remained elusive. In order to understand how
49 Env is assembled on virions and how it differs structurally from soluble trimers, we carried out
50 cryo-electron tomography (cryo-ET) with sub-tomogram averaging, and structural mass
51 spectrometry analysis of native Env displayed on immature and mature Gag-bearing HIV-1 virus-
52 like particles. These studies advance our knowledge of native Env via insights gained from cryo-
53 ET of intact viral particles.
54
55 **Results and Discussion:**
56 Virion particles bearing ADA.CM Env, a variant of subtype B isolate ADA that was
57 selected for stability (Leaman and Zwick 2013), were produced in human HEK 293T cells as
58 previously described (Stano, Leaman et al. 2017) (Figure 1A, B). These membrane enveloped
59 virus-like particles, referred to as high Env (h)VLPs, display elevated levels of Env trimers that
60 are fully functional for mediating receptor binding and entry. Env on hVLPs retain the antigenic
61 profile of full-length Env (Figure S1 and Table S1), despite a C-terminal truncation of 102 amino
62 acids in CTD (Stano, Leaman et al. 2017). hVLPs assemble around a functional Gag layer that
63 undergoes proteolytic maturation and thus, have the composition of authentic HIV-1 virions, but
64 are replication incompetent because the packaged genome lacks the Env gene (Leaman and Zwick
65 2013, Stano, Leaman et al. 2017). Purified hVLPs were treated with aldrithiol-2 (AT-2), which
66 interrupts nucleocapsid interaction with RNA, to ensure non-infectivity (Rossio, Esser et al. 1998).
67 Antibody binding experiments showed that the antigenicity of hVLP-Env was unaffected by AT-
68 2 treatment (Figure S2), suggesting the hVLP-Env trimer conformation is unaltered by AT-2,
69 which is in contrast to a recent report for a neutralization sensitive HIV Env (Li, Li et al. 2020).

70 The high density of surface Env on hVLPs allowed us to gather sufficient cryo-ET data to obtain
71 a 9.1Å resolution structure of native Env in its authentic context on virus-like particles (Figure 1C
72 and S3).
73
74 **Env structure from immature particles reveal interactions with Gag**
75 Though the hVLPs in our sample population were predominantly mature, we also observed
76 particles at different stages of maturation (Figure 1D). Approximately 3% of the particles were
77 fully immature, exhibiting a clear, assembled Gag lattice beneath the viral membrane (Figure 1A,
78 D). Env sub-tomogram volumes from only immature particles were averaged together to give
79 density maps at ~31 Å (C3 symmetry) and ~34 Å (C1 symmetry) (Figure 2A and S4). The Env
80 structure from immature particles closely resembles the sub-nanometer Env structure generated
81 from the total hVLP population (Figure 1C) and other reported Env ectodomain structures (Kwon,
82 Pancera et al. 2015, Ward and Wilson 2015). In the averaged immature Env map, a third density
83 layer is seen underneath the membrane bilayer corresponding to the Gag lattice position (Figure
84 1A, 2A, B and Figure S4B, C). Focused refinement of this internal third layer revealed a distinct
85 structure that clearly resembles a lattice formed by the capsid domain (CA) of immature Gag
86 polyprotein (Figure 2B and Figure S4D) (Schur, Hagen et al. 2015). Thus, structures of trimeric
87 Env ectodomain (Pan, Peng et al. 2020) and hexameric Gag-CA (Schur, Hagen et al. 2015) were
88 fitted as rigid bodies into corresponding densities in the averaged map (Figure 2C). No clear
89 density for the Env TMD-CTD was observed in the averaged structure, even though the TMD is
90 seen in individual raw tomograms (Figure 2C), suggesting that the TMD is not strictly aligned
91 with the ectodomain or Gag-CA. The structure of the TMD-CTD (PDB ID: 6UJV) was thus placed
92 into the map based on its position relative to the Env ectodomain (Figure 2C) (Piai, Fu et al. 2020).

93 The N-terminal MA domain of immature Gag polyprotein assembles along the inner
94 membrane leaflet as a hexameric lattice of trimers (Frank, Narayan et al. 2015, Tedbury, Novikova
95 et al. 2016) and is connected by a flexible linker to the Gag-CA lattice underneath (Tedbury and
96 Freed 2014). Although regularly spaced puncta corresponding to the Gag-MA domain can be
97 discerned directly underneath the inner leaflet and Env ectodomains in immature hVLP tomograms
98 (Figure 2C), distinguishable density for the Gag-MA layer was not seen in the averaged immature
99 map implying that the Gag-MA lattice (Tedbury and Freed 2014, Frank, Narayan et al. 2015,
100 Tedbury, Novikova et al. 2016), may have subtle variations in arrangement that deviate from Gag-
101 CA or Env symmetry axes. Hence, based on the expected position of Gag-MA relative to the Gag-
102 CA lattice (Frank, Narayan et al. 2015, Tedbury, Novikova et al. 2016), the MA lattice structure
103 was placed into the map (Figure 2C). As a result, juxtaposition of Env CTD and Gag-MA occurs
104 right at the bottom of the inner membrane as would be expected from the raw tomograms (Figure
105 2C). From this composite model, the relative position of Env CTD, when viewed normal to the
106 membrane, is on the rim of the hexameric Gag-CA lattice along its 2-fold axis (Fig2D). This
107 observation can also be corroborated in the raw tomograms (Figure 2E). Thus, the trimeric Env
108 CTD does not lie in the central hole formed by the immature Gag lattice as has been hypothesized
109 (Tedbury and Freed 2014, Tedbury, Novikova et al. 2016), but instead is positioned on its
110 hexameric rim (Figure 2D, F). In this configuration, the modeled Env CTD makes direct contact
111 with critical residues on MA previously shown to be necessary for Env incorporation in virions
112 (Figure 2F) (Tedbury and Freed 2014, Tedbury, Novikova et al. 2016).
113
114
115

116 **Rearrangement of MA layer occurs during maturation**

117 In immature particles, the Gag-MA layer is consistently arrayed underneath the inner
118 membrane (Figure 1A, D and 2C), whereas in mature particles where the Gag polyprotein has been
119 proteolytically cleaved, the MA layer appears fragmented (Figure 2G), indicating that MA
120 rearranges during particle maturation. Notably, Env trimers in the mature particles are not
121 colocalized with the MA layer (Figure 2G). Given this ultrastructural reorganization following
122 maturation, it seems possible that disruption of membrane-associated Gag lattices may be a
123 prerequisite for Env trimers to gain necessary mobility to mediate membrane fusion (Wyma, Jiang
124 et al. 2004, Roy, Chan et al. 2013). These structural changes may also provide sufficient membrane
125 pliability for remodeling during viral fusion, similar to matrix layer disruptions seen in other
126 viruses such as influenza virus (Gui, Ebner et al. 2016).

127

128 **Sub-nanometer HIV-1 Env structure shows a conformationally variable gp41 subunit**

129 A total of 32802 sub-volumes were used to reconstruct a C3-symmetric sub-tomogram
130 averaged structure of hVLP-Env with local resolution ranging between 5.7 -12 Å and a global
131 resolution of 9.1 Å (Figure 1C, 3A, B and Figure S3) (Table 1). Classification of the sub-volumes
132 did not yield any other distinct conformational class, indicating that the hVLP-Env were in a
133 predominantly closed, pre-fusion state. The Env ectodomain connects to the membrane via a thin
134 tripod stalk (Figure 1C and 3B). Though the TMD can be observed spanning the membrane layer
135 in raw tomograms (Figure 1A), no evidence of TMD is seen in the sub-tomogram averaged
136 structure (Figure 3B), similar to the Env structure from immature hVLPs.

137 Hydrogen-deuterium exchange mass-spectroscopy (HDX-MS) analysis of hVLP-Env from
138 intact particles showed that key fiducial peptides which report on trimer integrity (Guttman, Kahn

139 et al. 2012, Guttman, Garcia et al. 2014), were well-protected in hVLP-Env (Figure 3C),
140 confirming its closed, pre-fusion conformation. Relative to standard HDX-MS experimental
141 approaches, we were able to improve peptide coverage by performing deuterium exchanges under
142 native conditions but solubilizing the surface protein using detergent under quench conditions
143 (Figure S5). Comparison of hVLP-Env with BG505.SOSIP showed that cognate peptides
144 throughout the trimers had similar exchange profiles (Figure S6), indicating that they both have
145 comparable global conformations. However, the hVLP-Env trimer on virions exhibited greater
146 exchange protection, indicating it is in general more structurally ordered than the engineered
147 soluble trimer (Figure 3C and S6). Indeed, in terms of gp120 subunit organization, hVLP-Env has
148 a global architecture that closely resembles previously published Env structures (Kwon, Pancera
149 et al. 2015, Ward and Wilson 2015, Lee, Ozorowski et al. 2016, Pan, Peng et al. 2020). This is
150 confirmed by good agreement seen in fitting the atomic structure of detergent extracted full-length
151 Env (PDB ID: 6ULC) into the sub-tomogram averaged map (Figure 3A, B).
152
153 **Differences in gp41's terminal HR2 helix and stalk influence MPER surface exposure**
154 Significant differences relative to available structures are evident, however, in the gp41
155 subunit of hVLP-Env. In nearly all known Env structures, the HR2 helix has a long, rod-like
156 conformation with Asp664 forming its distal tip (Kwon, Pancera et al. 2015, Ward and Wilson
157 2015). In contrast, in hVLP-Env, Gln-653 forms the distal tip of the HR2 helix, making the helix
158 length 10 amino acids shorter (Figure 3B). The remaining residues in the C-terminal portion of
159 HR2 helix bend and form a thin stalk connecting the ectodomain to the membrane (Figure 3B).
160 Apart from hVLP-Env, this bend in HR2 helix has only been observed in the full-length, detergent-
161 solubilized Env structure derived from strain 92UG037.8 (Pan, Peng et al. 2020). In the presence

162 of membrane, we observe that the thin stalks, corresponding to Env residues 654-664, form a tripod
163 that elevates the ectodomain ~10 Å above the membrane (Figure 3B). As a result, the bulk of the
164 MPER (Membrane-Proximal External Region) (residues 660-683), which is a desirable vaccine
165 target of some of the most broadly neutralizing HIV-1 antibodies isolated to date (Gray, Madiga
166 et al. 2009, Rantalainen, Berndsen et al. 2020), is primarily embedded within the membrane in our
167 structure.

168 The complete MPER peptide is unresolved in all reported structures of trimeric Env, owing
169 to its membrane proximal location and/or possible variations in its conformation. Current
170 knowledge of MPER structure is only derived from constructs without the Env ectodomain
171 included (Fu, Shaik et al. 2018, Piai, Fu et al. 2020). In a recently published structure of Env from
172 BaL-1 virions, MPER was indicated to form part of the stalk connecting Env ectodomain to the
173 membrane (Li, Li et al. 2020), which contrasts with the membrane embedded MPER location
174 identified in our structure (Figure S7). However, the embedded nature of the MPER in our map is
175 in agreement with that inferred from other solubilized full-length Env structures and biophysical
176 studies on binding of MPER-targeted antibodies to HIV-1 Env (Kim, Sun et al. 2011, Lee,
177 Ozorowski et al. 2016, Wang, Kaur et al. 2019, Rantalainen, Berndsen et al. 2020). Analyzing Env
178 structures from different HIV strains shows that the general position of the bulk of the ectodomain
179 is ~10-12 Å above the interpreted membrane surface in all cases (Figure S7). However, differences
180 arise in the position of HR2 helix and subsequent MPER sequence leading to variability in MPER
181 presentation and accessibility above the membrane amongst HIV-1 strains.
182
183
184

185 **A flexible gp41 stalk allows Env orientational freedom and MPER epitope exposure**

186 In our tomographic data, we observe tilting of hVLP-Env with respect to the membrane
187 (Figure 4A), which leads to a lower density level for the stalk in our sub-tomogram averaged map
188 (Figure 4B). Thus, the tripod stalk of Env is flexible in its native state, allowing differential
189 sampling of MPER and other membrane-proximal epitopes. Although tilting or lifting of Env from
190 the membrane on binding to MPER targeted antibody 10E8 (Lee, Ozorowski et al. 2016,
191 Rantalainen, Berndsen et al. 2020) and gp120-gp41 interface targeting antibody 35O22 (Huang,
192 Kang et al. 2014) has been suggested, our results provide the first direct evidence of Env tilting on
193 native membrane in its natural, unliganded state.

194 Sensitivity to MPER broadly neutralizing antibodies (bnAbs) has been shown to be
195 impacted by Env stability in its prefusion state (Kim, Leaman et al. 2014), with increased
196 neutralization observed after cellular receptor engagement (Frey, Peng et al. 2008, Chakrabarti,
197 Walker et al. 2011). Based on the structural data discussed above, we envision that local structure
198 of HR2, height of the Env ectodomain above membrane, and propensity of Env tilting have
199 additional impact on Env sensitivity or resistance to MPER bnAbs. To test this hypothesis, we
200 conducted comparative neutralization assays using MPER bnAbs against HIV-1 strains whose Env
201 structures have been determined. As anticipated from the structural data, amongst the three viruses,
202 ADA.CM hVLP, BaL-1 and BG505, ADA.CM was overall more resistant to MPER bnAbs (Figure
203 4C and Table S2). Neutralization and mutational analysis of proximal residues in ADA.CM that
204 contribute to trimer stability (Figure S8) showed modest individual effects but none were
205 individually responsible for ADA.CM's enhanced resistance to MPER bnAbs (Figure S8 and
206 Table S3).

207

208 **Structural variation in gp41's HR1-C helical bundle suggests a conformationally variable**
209 **central core**

210 Another prominent difference in the gp41 subunit of hVLP-Env is absence of complete
211 density for the central C-terminal HR1 helices (HR1-C) (Figure 5A). The HR1-C helices
212 comprised of amino acid residues 570-595 have been a hallmark of high resolution Env SOSIP
213 structures with the central trimeric bundle composed of a HR1-C helix from each of the gp41
214 domains. However, in our structure, only partial density for the HR1-C helix can be observed
215 corresponding to gp41 residues 570-577 and 582-595 (Figure 5A). Classification of Env sub-
216 volumes with a tight cylindrical mask for the gp41 region did not yield any subset with higher
217 density for HR1-C helices in our data. Considering that our sub-tomogram averaged map has a
218 local resolution range for the ectodomain between 5.7-12 Å (Figure S3), it is clear from
219 comparisons with other cryo-EM maps at similar resolutions, that the absence of complete HR1-
220 C helix density in our structure is not an effect of map resolution (Figure S9).

221 To ascertain whether the observed HR1-C density was affected by applied symmetry to the
222 map, we calculated an asymmetric structure of hVLP-Env at 10.7 Å resolution (Figure S3 and
223 Table 1). The asymmetric structure (Figure 5B) appears overall similar to the three-fold
224 symmetrized map (Figure 5A). Partial density for the HR1-C helices is consistently present across
225 all three protomers in the asymmetric structure, with near-complete density for HR1-C observed
226 in one protomer (Figure 5B).

227 HDX-MS analysis provides additional insight into the state of this key structural motif.
228 Peptides in HR1-C helix (residues 570-579 and 583-593) are more protected in hVLPs than in
229 BG505.SOSIP (Figure 5C), indicating increased backbone hydrogen bonding interactions in
230 corresponding residues. Taken together, the sub-tomogram averaged structures and HDX-MS

231 analysis shows that the peptides in HR1-C region exist in a stable, ordered conformation in hVLP-
232 Env even though they do not rigidly conform to Env's global three-fold structural symmetry.
233
234 **An extensive and heterogenous glycan shield in hVLP-Env protects critical epitopes**
235 The hVLP-Env structure displays distinguishable density features for N-linked glycans that
236 decorate the ectodomain surface. In contrast to most available structures where density near to
237 glycosylation sites often covers only the core GlcNAc sugars, in our unliganded hVLP-Env
238 structure, extended electron density for glycan moieties is observed across the protein. Resolved
239 density for multiple canonical glycan positions in gp120 and gp41 subunits extends beyond the
240 range of current structural models, revealing the extent of the 'glycan shield' (Figure 6A) (Wei,
241 Decker et al. 2003). Glycans surrounding a number of key bnAb epitopes can be identified in the
242 unliganded Env map, which reveal their orientations in the natural, antibody-naïve state so as to
243 occlude underlying epitopes.
244 At the CD4 receptor binding site (CD4bs) in hVLP-Env, overlaying the previously
245 determined Fab (Fragment antigen binding) structure of VRC01 (CD4bs bnAb) (Stewart-Jones,
246 Soto et al. 2016) in its binding orientation, highlights possible clashes with nearby glycans N197,
247 N276, N361 and N461 (Figure 6B). These glycans have also been shown to overlap with the
248 VRC01 epitope using molecular dynamic studies, but previously determined structures using
249 SOSIPs resolved only short glycan chains at these sites (except for N276) resulting in minimal
250 apparent glycan interactions with the bnAb (Stewart-Jones, Soto et al. 2016). In hVLP-Env,
251 extended density for these multiple glycans can be seen to clearly deter binding of CD4 epitope-
252 directed nAbs (Figure 6B). These observations are corroborated in VRC01 based neutralization
253 assays which show that hVLP-Env is substantially more resistant than BaL-1 Env (Figure 6B and

254 Table S2), whose structure lacks extended glycosylation around this site (Li, Li et al. 2020).
255 Indeed, removal of N276 and N461 glycans has been demonstrated to facilitate engagement of
256 germline precursor antibodies for VRC01-like nAbs that normally do not interact strongly with
257 natively glycosylated Env (McGuire, Hoot et al. 2013).

258 Similarly, long-range extended densities for N-linked glycans are observed in the gp41
259 domain corresponding to residues N262, N448, N611 and N637. The close spacing of N262/N448
260 to N611 likely orders them such that they are visible in the averaged map (Figure 6A, C).
261 Collectively, these glycans form a protective barrier over the fusion peptide (FP) in hVLP-Env
262 (Figure 6C). Env's FP is essential for viral cell entry but is surprisingly exposed to solution and
263 highly dynamic by HDX-MS analysis (Figure 5C). Mapping the Fab structure of FP targeting
264 bnAb, PGT151 (Lee, Ozorowski et al. 2016), onto its corresponding epitope on hVLP-Env shows
265 how the glycans would need to be displaced in order for the antibody to bind (Figure 6C). Though
266 hVLPs are neutralized by PGT151, they are relatively resistant compared to other strains (Figure
267 6C and Table S2), suggesting that glycan occlusion may impact neutralization by FP targeted
268 bnAbs as has been reported (Stewart-Jones, Soto et al. 2016).

269 Extensive glycan densities also persist in the asymmetric structure of hVLP-Env but
270 strikingly, we observe variations in densities between different protomers, indicating heterogeneity
271 in glycan occupancy. For example, the N355 glycan is present at all three protomers in the
272 asymmetric Env reconstruction but its density varies with respect to size and orientation at this site
273 (Figure 6D). Similarly, the conserved N88 glycan, which forms part of the epitope of bnAb 35O22
274 (Huang, Kang et al. 2014) and borders that of 10E8 (Lee, Ozorowski et al. 2016), can only be
275 observed in one protomer but not in others (Figure 6D) and is absent in the C3-symmetrized map.
276 In mass spectrometry analysis of hVLP-Env, these glycan sites, along with others, exhibit presence

277 of a heterogenous population of complex sugars (Table S4). Thus, though identified heterogeneity
278 in glycan processing of hVLP-Env (Table S4) is similar to previous reports (Guttman, Garcia et
279 al. 2014, Cao, Pauthner et al. 2018, Berndsen, Chakraborty et al. 2020); our comparative structural
280 analysis on asymmetric and symmetric hVLP-Env directly resolves glycan heterogeneity within
281 protomers of the same Env trimer.

282 When comparing bnAbs affected by both the presence of glycan and membrane proximity,
283 binding of bnAb 35O22 (Huang, Kang et al. 2014) is highly dependent on the presence of N88
284 glycan whereas 3BC176 binding (Lee, Leaman et al. 2015) is partially inhibited by it. Mapping
285 binding orientation of both these Fabs onto hVLP-Env results in steric clashing of the Fab regions
286 with the membrane surface (Figure 6E). Nevertheless, hVLPs are effectively neutralized by 35O22
287 but show relative resistance to 3BC176 (Figure 6E and Table S2), presumably due at least in part
288 to 3BC176's lower binding capacity (Lee, Leaman et al. 2015). Thus, a combination of
289 heterogenous presence of N88 glycan along with the ability of hVLP-Env to tilt on membrane can
290 account for differential access to these binding epitopes.

291

292 **Conclusions**

293 In this study, we have analyzed the structure of HIV particles displaying functional Env.
294 Although the ADA.CM Env trimers used are highly stable in a membrane environment, they
295 notably do not form well-ordered gp140 trimers in solution using the typically employed "SOSIP"
296 mutations (Leaman and Zwick 2013). This is true for the majority of Env sequences that require
297 extensive modifications in order to encourage formation of stable ectodomain trimers (Rawi,
298 Rutten et al. 2020). Thus, the structural details discussed here may reflect features of Env strains

299 that are not compatible with SOSIP modifications and thus have not been structurally characterized
300 so far.

301 In hVLP-Env, we find substantial evidence that key parts of gp41 including the HR1 central
302 helices and flexible stalk are not rigidly fixed relative to the rest of the trimer. Indeed, R.M.S.D.
303 calculations among static high-resolution structures of full-length Env and SOSIP structures show
304 higher deviation in the gp41 domain compared to gp120 domain (Table S5), despite the strains
305 having greater than 75% sequence similarity (Table S6). Likewise, DEER spectroscopy studies of
306 SOSIP trimers have also shown a higher degree of variability in the gp41 domain (Stadtmueller,
307 Bridges et al. 2018), further substantiating the flexible nature of gp41 as inferred from our
308 structures.

309 Our data also demonstrate that even in membrane associated Env, the fusion peptide (FP)
310 is highly dynamic and exposed to solvent. Exposure of such a functionally critical and conserved
311 component seems counter-intuitive, but the dense clustering of glycans around the FP proximal
312 region likely confers a degree of steric protection. However, breaches in the glycan shield, revealed
313 by heterogeneity in glycan density in this region in our structures, can still offer access to the FP
314 by bnAbs (Kong, Xu et al. 2016, Lee, Ozorowski et al. 2016). Moreover, in cases where glycans
315 form part of bnAb epitopes, heterogeneity in glycosylation provide mechanisms exploited by HIV-
316 1 as a means of increasing epitope variability and facilitating evasion of antibody responses.
317 Finally, the extent of ordered density between adjacent glycans in hVLP-Env suggests that the
318 glycans are interacting in a stable manner, consistent with recent reports (Stewart-Jones, Soto et
319 al. 2016, Berndsen, Chakraborty et al. 2020).

320 By imaging Env in its native membrane-bound context, we found that, like other type I
321 fusion proteins such as SARS-CoV-2 S trimers (Ke, Oton et al. 2020), HIV-1 Env ectodomain sits

322 atop a flexible stalk that affords it considerable freedom of motion to tilt relative to the membrane.
323 This likely plays an important mechanistic role by affording fusion proteins the flexibility to bind
324 receptors and refold during membrane fusion. The flexible stalk also impacts the accessibility of
325 key epitopes that are sterically hindered on the membrane-facing side of the trimer ectodomain
326 such as the FP, gp120/gp41 interface, and membrane-associated MPER. Thus, our structural
327 analyses revealed previously uncharacterized Env features that impact presentation of prime
328 epitopes which can help explain differences in neutralization sensitivity across diverse HIV-1
329 strains.

330 Lastly, our structural analyses of Env in immature viral particles, shows that Env is situated
331 directly over two-fold symmetric contacts of the Gag lattice, providing the first structural evidence
332 of a direct physical Env-Gag interaction, helping to inform models for virion particle assembly
333 and Env incorporation. Taken together, our results advance understanding of native HIV-1 Env in
334 the context of virion assembly, maturation and conformational sampling, revealing insights that
335 are generally unavailable through structural studies on recombinant proteins alone.

336

337

338 **Acknowledgements:**

339 We thank the University of Washington Arnold and Mabel Beckman cryoEM center and the
340 School of Pharmacy mass spectrometry center for data collection time and support. This work
341 was supported by National Institutes of Health (NIAID) grants R01GM099989 and
342 R01AI140868 to K.K.L., T32 GM008268 to M.A.B., and R01AI143563 to M.B.Z., the James B.
343 Pendleton Charitable Trust (M.B.Z.), and by the University of Washington's Proteomics
344 Resource (UWPR95794).

Author Contributions: V.M.P.: Conceptualization, Formal analysis, Investigation, Validation and Writing.:D.P.L.: Investigation, Formal Analysis. K.N.L.: Investigation, Formal Analysis. M.A.B.: Investigation. E.A.H.: Investigation. M.B.Z.: Resources, Writing review, Funding acquisition. K.K.L.: Conceptualization, Writing, Funding acquisition.

Competing interests: Authors declare no competing interests;

Data Availability: Density maps with corresponding atomic models have been deposited with accession codes EMD-XXXX, EMD-XXX, EMD-XXX, EMD-XXXX and PDB IDs XXXX and XXX.

356 **Figures:**

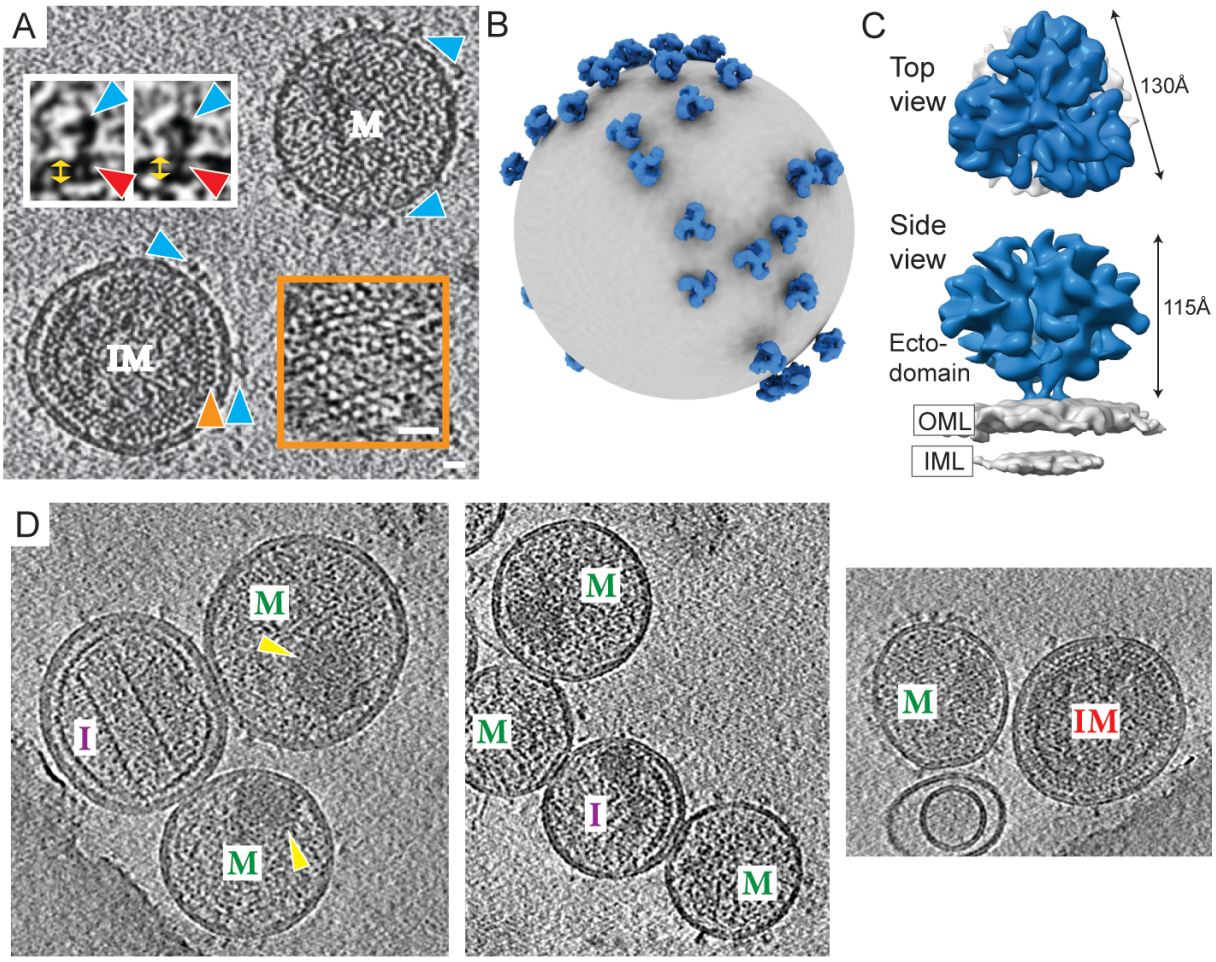

357

358 **Figure 1. Structural analysis of hVLP-Env. (A)** Tomogram slice showing a mature (M) and
359 immature hVLP (IM). Blue arrows indicate Env. Orange arrow indicates Gag layer in IM with
360 zoomed inset of Gag top view on bottom right. Scale bars indicate 200 Å. Top left inset shows
361 close-up of Env with red arrows denoting TMD and yellow arrows denoting membrane bilayer.
362 (For antigenic profile of hVLPs, see Figures S1 and S2). **(B)** Representative model of mature
363 hVLP with averaged Env structure (in blue) placed onto original particle coordinates. Membrane
364 surface is shown in grey. **(C)** Sub-tomogram averaged Env structure at 9.1Å resolution (for
365 resolution related statistics, see Figure S3). OML and IML indicate outer and inner membrane
366 leaflets, respectively. **(D)** Tomogram slices showing different maturation states observed in the

367 hVLP population. Immature particle showing a continuous Gag layer underneath the membrane
368 is labeled IM. Mature particles with the Gag layer reorganized into clearly formed internal capsid
369 is labeled M. Yellow arrows indicate the internal mature capsid in two representative virions.
370 Particles at intermediate stages of maturation are labeled I. Scale bar corresponds to 50 nm.
371 Black is high density in all panels.
372

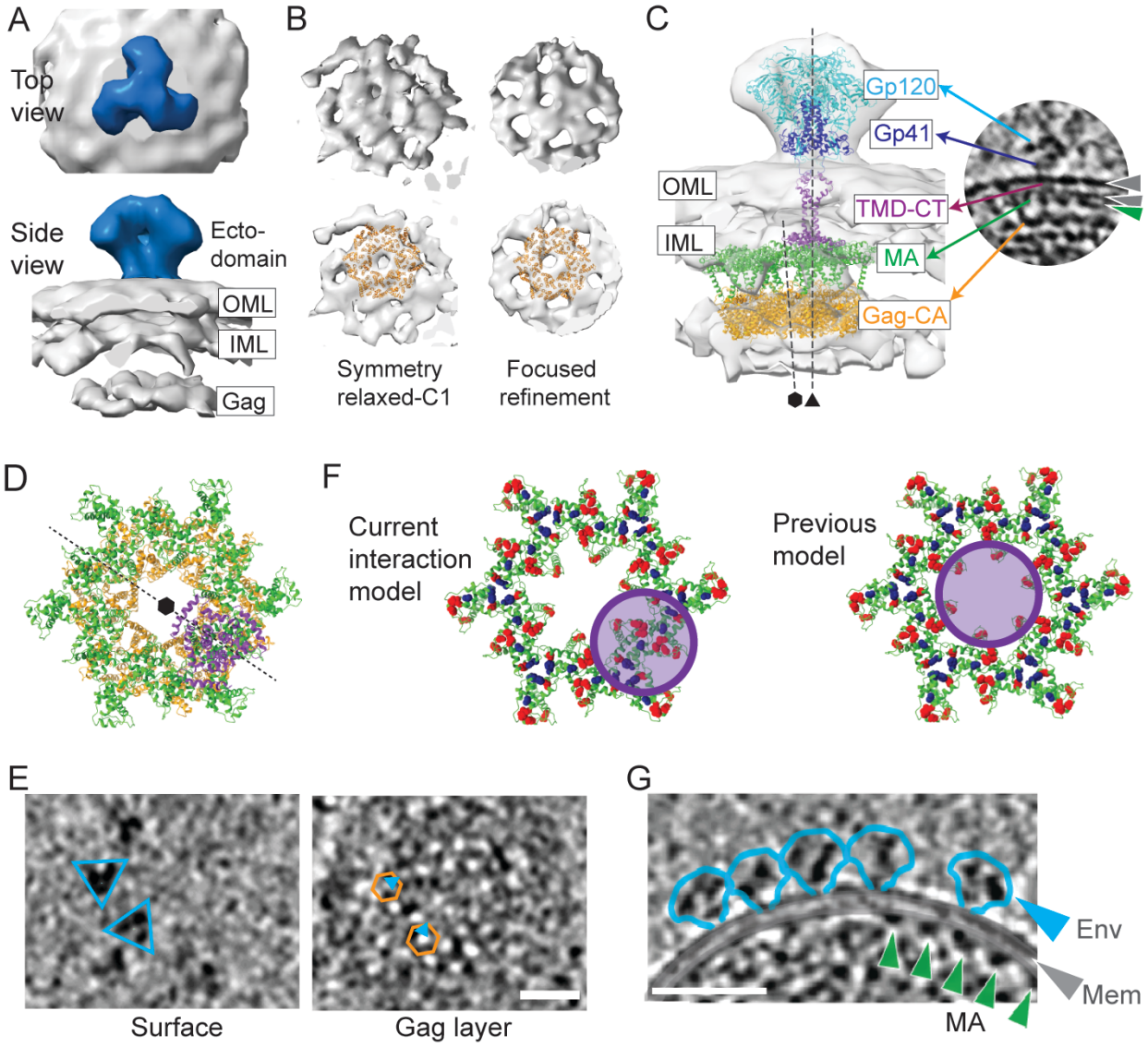

Figure 2. HIV Env interaction with immature Gag polyprotein. **(A)** Sub-tomogram averaged Env structure from immature VLPs. OML and IML indicate outer and inner membrane leaflets, respectively. (**B)** Top views of immature Gag layer from relaxed C1 symmetry map (top left) and after focused refinement (top right) (see Figure S4 for details). Bottom panels show the same with fitted atomic structure of hexameric Gag-CA (PDB: 4USN). (**C)** Left: Composite model of Env-Gag structures in immature particles. Atomic coordinates of Env ectodomain with Gp120 (cyan) and Gp41 (dark blue), TMD and CTD in purple (PDB: 6UJV), Gag-MA hexamer (PDB: 1HIW) in green and Gag-CA hexamer in orange are shown. Right: Tomogram slice of Env from

382 an immature particle with protein components labeled. Grey and green arrows indicate
383 membrane bilayer and Gag-MA respectively. (**D)** Top view of CTD (purple) and Gag-MA-CA
384 (green) interface. CTD lies on the 2-fold axis (black line) of underlying Gag-CA hexamer
385 (orange). (**E)** Left: Tomogram cross-section of immature VLP surface showing Env positions
386 (blue triangles). Right: Position of Env central axis (blue triangles) with respect to the Gag-CA
387 hexamer (orange hexagon) is shown when viewing along an axis perpendicular to the plane of
388 image. Env position superposes on the edge of Gag hexamer. Black represents high density.
389 Scale bar is 200 Å in length. **(F)** Model of Env-CTD interaction with Gag-MA. Ribbon diagram
390 of Gag-MA hexamer (green) (PDB ID: 1HIW) (Hill, Worthylake et al. 1996) is shown. Residues
391 that reduce Env incorporation when mutated (13L, 17E, 31L, 35V, 99E and 75LG) are
392 highlighted as red spheres (Alfadhli, Staubus et al. 2019). Residues that reportedly suppress Env
393 incorporation defects (62QR, 35VI and 44FL) are shown as blue spheres (Alfadhli, Staubus et al.
394 2019). Position and area covered by Env CTD structure (based on PDB ID: 6UJV (Piai, Fu et al.
395 2020)) in our current model (left) and previously predicted models (right) is shown as purple
396 circle. In previous models (right panel), Env CTD position was predicted to be at the center of
397 the Gag-MA hexamer. In this configuration, Env CTD directly interacts with only a few residues
398 that line the inner circumference of Gag-MA hexamer. Thus, the effect of the majority of
399 involved residues on Env incorporation would be allosteric. In the current model (left panel)
400 based on our cryo-ET data, the Env CTD position encompasses all residues determined to affect
401 Env incorporation, giving rise to direct contacts between Env CTD and Gag-MA residues. (**G)**
402 Cross-section of mature VLP shows the presence of Env (blue) on membrane surface (grey)
403 irrespective of the presence of visible MA density (green) underneath. Scale bars are 200Å.
404

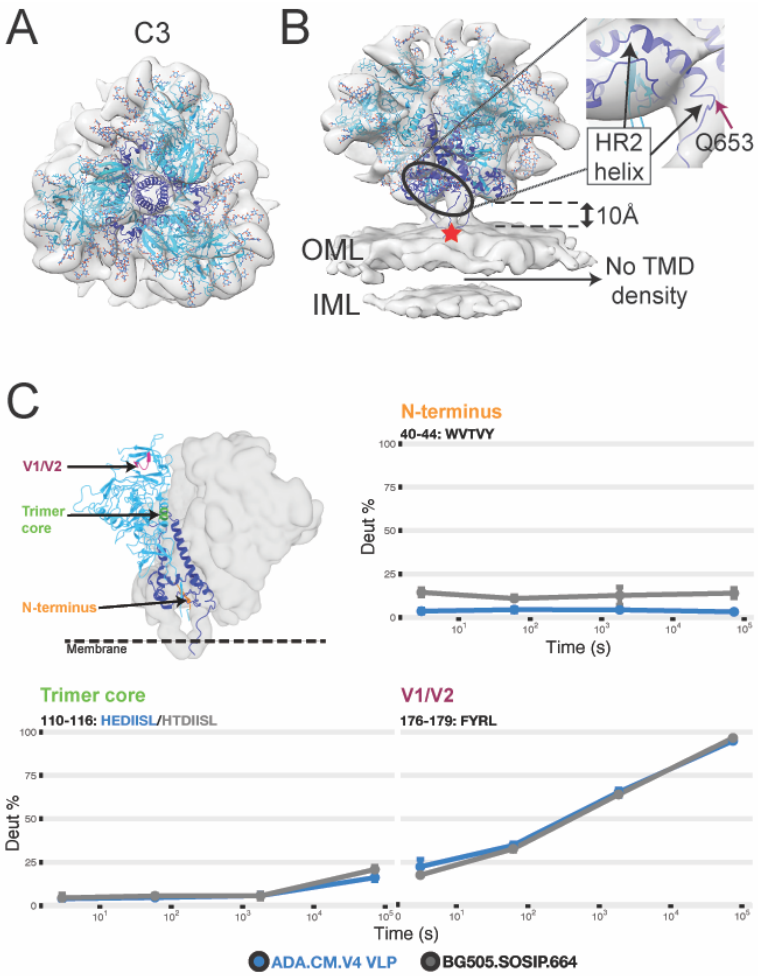

405

406 **Figure 3. Sub-nanometer structure of hVLP-Env indicates conformational variation in HR2**
407 **helix and MPER location.** Top **(A)** and side-view **(B)** of sub-tomogram averaged Env map with
408 fitted ribbon structure adapted from full-length Env structure (PDB ID: 6ULC). Gp120 subunit is
409 colored in cyan, gp41 in dark blue, glycans are colored as red and blue heteroatoms. Outer and
410 inner membrane leaflets are indicated as OML and IML respectively. Zoomed inset shows the
411 shortened HR2 helix fitted into its respective density. Red star indicates position of Asp-664 in the
412 trimer structure (See Figure S7 for details on MPER variation). **(C)** HDX-MS of hVLP-Env shows
413 protection of peptides that report on the closed prefusion conformation of HIV-1 Env (Guttman,
414 Garcia et al. 2014, Guttman, Cupo et al. 2015) (see also Figures S5 and S6). Deuterium uptake for

415 peptides reporting on trimer integrity behave similarly between hVLP-Env and BG505.SOSIP,

416 which predominantly samples a closed prefusion conformation.

417

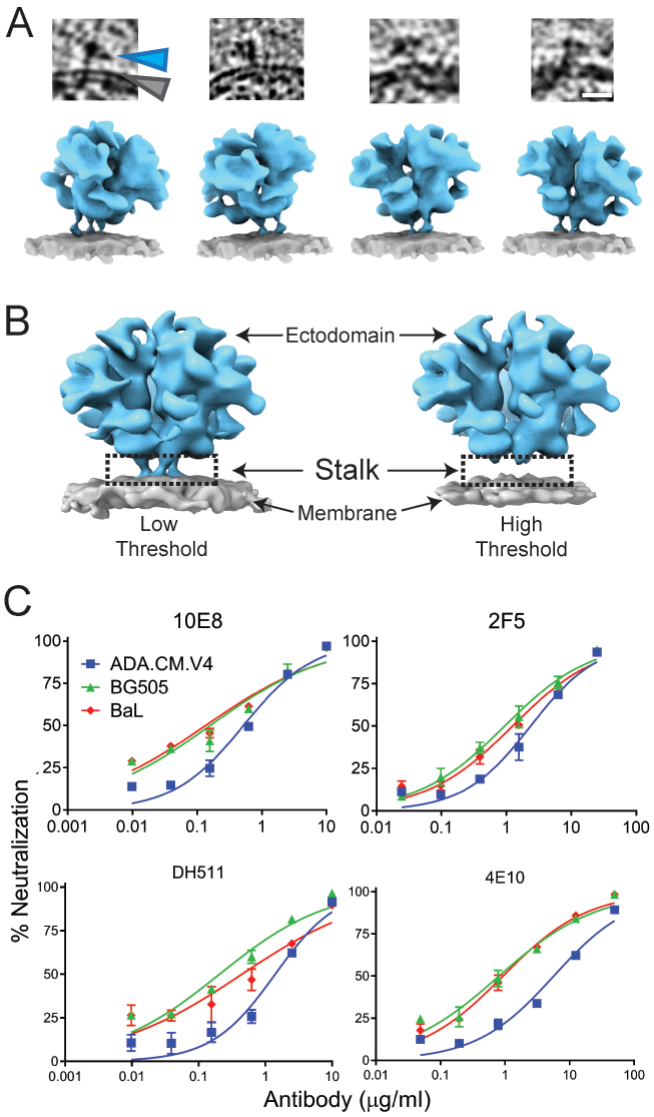

418

419 **Figure 4. Flexible gp41 stalk in HIV Env leads to variation in MPER epitope accessibility.**
420 **(A)** Top: Tomogram slices showing examples of tilted Env on membrane surface. Scale bar equals
421 100 Å. Bottom: Surface rendering of modeled Env structure (blue) in tilted orientations on
422 membrane (grey) as seen in the tomograms. **(B)** Env density map rendered at low and high
423 thresholds, respectively, showing loss of density in the stalk region (black rectangle). **(C)**
424 Comparison of neutralization effect on different HIV-1 strains by MPER-directed bnAbs. Also see
425 Figure S8.

426

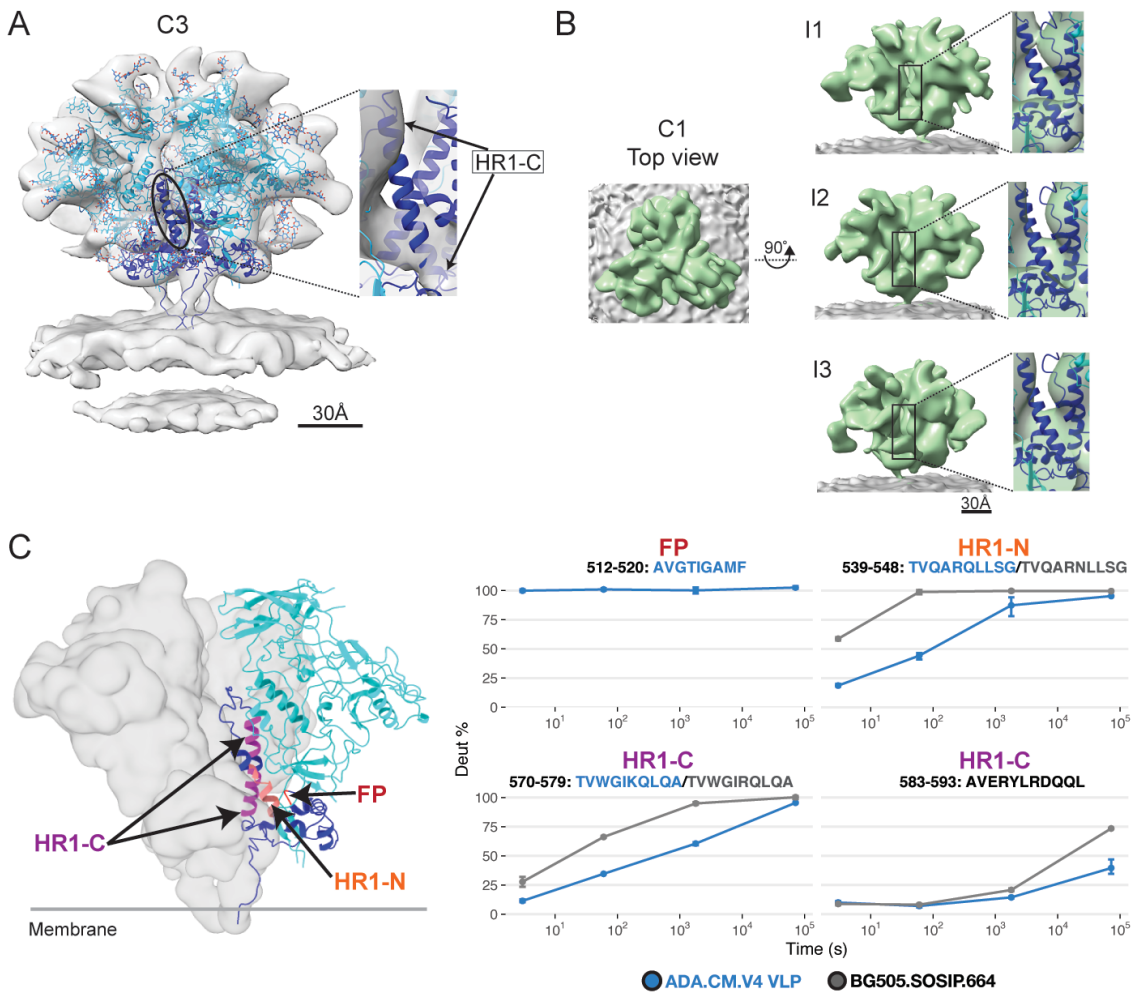

Figure 5. Conformational variation in central helical bundle (HR1-C) of hVLP-Env. A) Side-view of sub-tomogram averaged Env map with fitted ribbon structure and colored similar to Fig. 2. Zoomed inset shows fit of HR1-C helix into its respective density (See also Figure S9). **B)** Top and side views of an asymmetric reconstruction of hVLP-Env with the three interfaces (I1, I2 and I3) of Env trimer shown along with magnified insets of fitted HR1-C helix. Black, dotted rectangle indicate the central core of the trimer where the HR1-C helix lies. See Figure S3 for resolution-related details. **C**) HDX-MS deuterium uptake plots for fusion peptide (FP) and HR1 peptides (see also Figures S5 and S6). Surface rendering of Env was calculated using the fitted atomic model of hVLP-Env in panel A without glycans. Full FP region is not observed in hVLP-Env structure due to flexibility.

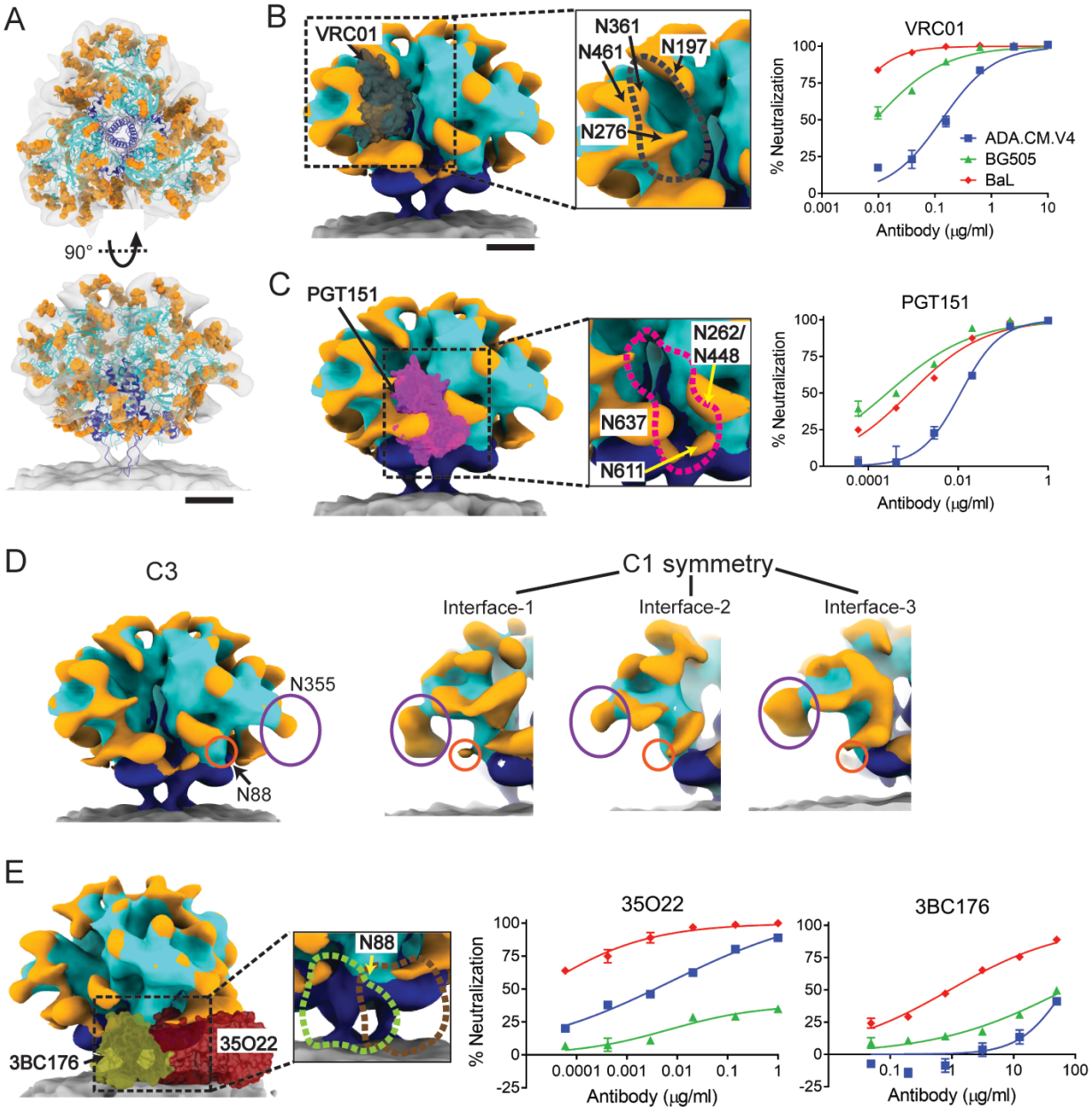

Figure 6. Presence of an extensive glycan shield in hVLP-Env. **A)** Top and side view of hVLP-Env with glycans rendered as orange ball-stick structures. Gp41 colored in dark blue and gp120 in cyan. **B), C)** and **E**) Binding positions of four bnAbs – VRC01 (dark grey), PGT151 (pink), 35O22 (brown) and 3BC176 (green) mapped onto hVLP-Env surface. Gp120, gp41, glycan surfaces and membrane are colored in cyan, dark blue, orange and grey respectively. Zoomed-in sub-panel outlines interaction surfaces corresponding to each bnAb. Glycans that

445 would obstruct bnAb binding are labeled. Neutralization of HIV-1 strains, ADA.CM.V4, BG505
446 and BaL in presence of each bnAb are shown. **D)** Differential glycosylation among trimer
447 subunits in hVLP-Env represented using glycans at N88 (orange circle) and N355 (purple oval).
448 Surface rendering of C3-symmetrized map on left followed by the three protomer interfaces from
449 the C1 symmetry hVLP-Env map. Scale bars equal 30 Å.

450 **Table 1**.

451 Data collection and processing parameters for cryo-ET and sub-tomogram averaging.

Data Collection Parameters:				
Magnification	58000X			
Voltage	300 kV			
Pixel size	2.58 Å/pixel			
Electron dose	64-68 $e^-/Å^2$			
Defocus Range (µm)	-2.5 to -5.0			
Total number of tilt-series	526			
Final number of tilt-series	423			
Data Processing Parameters:				
	hVLP-Env C3 symmetry (sym)	hVLP-Env C1 sym	Immature hVLP-Env C3 sym	Immature hVLP-Env C1 sym
Initial number of sub-volumes	63592	63592	1520	1520
Final number of sub-volumes	32802	29074	1051	1059
Map resolution at 0.143 FSC	9.13 Å	10.67 Å	31.35 Å	34.3 Å

452

453 **Experimental Methods:**

454 hVLP expression and purification:

455 Stable cell line expressing high levels of HIV Env, ADA.CM.V4, was described previously (Stano,
456 Leaman et al. 2017). A stable cell line expressing Env BG505 was generated using a similar
457 method, namely by transduction of HEK293T cells using a lentiviral vector
458 (pLentiIII.BG505.755*) containing the *env* gene BG505 with a stop codon at position 756.
459 Transduced cells were subjected to two rounds of sorting by FACS using fluorescently labeled
460 quaternary neutralizing antibody PGT145 and non-neutralizing CD4BS antibody b6, then gating
461 cells for PGT145^{high} b6^{low}. Env copy number on BG505 VLPs was notably lower than on
462 ADA.CM.V4 hVLPs. Additionally, BG505 VLPs were also more fragile, which precluded
463 extensive cryo-ET data collection and HDX-MS analysis.

464 To generate hVLPs, cells were transfected using Env-deficient HIV-1 backbone plasmid
465 pSG3ΔEnv (NIH ARRRP) and 25 kDa PEI (Polysciences) as a transfection reagent. Supernatants
466 were harvested 3 days after transfection and cleared by centrifugation at 3,000 × *g* for 15 min.
467 hVLPs were pelleted at 80,000 × *g* for 1 h and resuspended 100-fold concentrated in PBS. VLPs
468 were separated from cellular debris using iodixanol density gradient centrifugation. Here,
469 concentrated hVLPs were overlaid on a 9.6 to 20.4% iodixanol (Optiprep; Sigma) gradient, formed
470 by layering iodixanol in 1.2% increments, and centrifuged at 200,000 × *g* for 1.5 h at 4°C in an
471 SW41Ti rotor (Beckman). Fractions (1 ml each) were collected starting from the top and fractions
472 6-9 were saved and pooled. Purified hVLPs were brought up to 15 ml with PBS and concentrated
473 to ~0.2 ml using a 100 kDa MWCO Amicon centrifugal filter (Millipore). VLPs were inactivated
474 by adding aldrithiol-2 (AT-2) to a final concentration of 2.5 mM and samples were incubated at
475 RT for 2 h. The volume was again increased to 15 ml with PBS and hVLPs were concentrated

476 using a 100 kDa MWCO centrifugal filter to 250-fold the concentration in the original transfection
477 supernatant.
478
479 Cryo-ET sample preparation and tilt-series acquisition:
480 Purified hVLP samples were mixed with 10nm gold beads (Aurion BSA Gold Tracer 10nm) at a
481 ratio of 15:1 (v/v). Using a Vitrobot Mark IV (FEI Co.), 3 µl of this mixture was applied to glow
482 discharged, C-Flat 1.2/1.3, 200mesh or 400mesh grids (Electron Microscopy Sciences), blotted for
483 4-5 seconds and plunge frozen in liquid ethane. Vitrobot was maintained at 4°C and 100%
484 humidity during the experiment.
485 Frozen grids were imaged using a 300 kV Titan Krios with a Gatan K2 direct electron
486 detector and GIF energy filter with slit width of 20 eV. Tilt-series were collected in a dose-
487 symmetric tilting scheme from -54° to +54° or from -48° to +48° with a step size of 3° using
488 Leginon (Carragher, Kisseberth et al. 2000) or SerialEM softwares (Mastronarde 2005). Tilt-series
489 were collected in counting mode at a magnification of 53000X, corresponding to a pixel size of
490 2.58 Å per pixel. The total dose per tilt series was ~64-68 $e^-/Å^2$. A total of 526 tilt-series were
491 collected across multiple sessions.
492
493 Tomogram reconstruction:
494 Tilt-series image frames were corrected for beam-induced motion using motioncor2 (Zheng,
495 Palovcak et al. 2017). Using batch tomography via the Etomo interface in IMOD software package
496 (Kremer, Mastronarde et al. 1996, Mastronarde and Held 2017), tilt-series were processed for
497 tomogram generation using standard procedures. Tilt series images were aligned using gold bead
498 markers and aligned tilt-series were used to generate a three-dimensional volume using weighted

499 back-projection method. The final tomograms were rotated, binned, and low pass–filtered for
500 visualization. Tilt-series with non-optimal alignments were discarded. In the end, 423 tilt-series
501 were selected for further processing.
502
503 Initial model generation:
504 Eight tilt-series were randomly selected. CTF estimation and correction for these were done using
505 the Ctfplotter program (Xiong, Morphew et al. 2009). Tomograms were then generated for these
506 CTF-corrected tilt-series in IMOD at the unbinned pixel size (Kremer, Mastronarde et al. 1996,
507 Mastronarde and Held 2017). The aligned tilt-series, reconstructed tomograms, file listing the tilt
508 angles and electron dose values were imported into Relion software suite (Scheres 2012) according
509 to its conventions (Bharat and Scheres 2016). Using the 3dmod graphical user interface (Kremer,
510 Mastronarde et al. 1996), 2067 Env particles on the surface of hVLPs were manually picked. The
511 picked particle coordinates were imported into Relion (Scheres 2012) and corresponding sub-
512 volumes extracted. These were then subjected to 3D classification with a spherical mask covering
513 small parts of the membrane using C1 and C3 symmetry with no initial model provided. Both the
514 C1 and C3 symmetry classifications resolved a 3D class that looked similar to the expected
515 structure of HIV-1 Env. The 3D class from the C3 symmetry run showing clear Env density
516 contained a total of 811 sub-volumes and was selected as initial model.
517
518 Sub-tomogram averaging:
519 For C3-symmetrized hVLP-Env structure:
520 Tilt-series were imported into EMAN2's sub-tomogram averaging pipeline (Chen, Bell et al.
521 2019). 1k X 1k tomograms were generated within EMAN2 using default parameters. The binned

522 tomograms were then used for semi-automated particle picking in PEET software (Nicastro,
523 Schwartz et al. 2006). Consolidated particles from the semi-automated picking were further
524 curated manually using the 3dmod interface (Kremer, Mastronarde et al. 1996) to remove wrongly
525 positioned particle points such as those that were in the membrane or on the inside of VLPs.
526 Curated particle coordinates (63592 particles) were then imported into EMAN2 through the
527 e2spt_boxer.py interface (Chen, Bell et al. 2019). CTF-estimation for all the tilt-series and
528 subsequent CTF-corrections were carried out within EMAN2. Sub-volumes were initially
529 extracted at 4xbinning corresponding to a pixel size of 10.32 Å per pixel. Sub-tomogram
530 refinement was carried using a spherical mask including Env on surface and a part of the
531 membrane. The 3D structure previously generated in Relion (Scheres 2012, Bharat and Scheres
532 2016) was used as initial model after low pass filtering to 60 Å. Sub-volumes were then re-
533 extracted at 2X binning using the particle orientations from the 4X binned refinement output. Sub-
534 tomogram refinement was repeated using the 2X binned data with a cylindrical mask covering
535 only the ectodomain and outer membrane layer. Particle orientations were locally refined within a
536 30º angular limit from the positions calculated in the 4Xbin refinement. Sub-volumes closer than
537 120 Å when measured between centers were removed. Sub-volumes with low cross-correlation
538 scores were also removed according to EMAN2's default settings. Remaining particles were then
539 re-extracted at the original, un-binned pixel size and re-refined starting from previously determined
540 orientations at 2X binning. Sub-tilt refinement in EMAN2 was then carried out using default
541 parameters following sub-tomogram refinement with un-binned sub-volumes (Chen, Bell et al.
542 2019). For sub-tilt refinement, a threshold mask was used that enclosed only the Env ectodomain
543 portion without any membrane density. The threshold mask was generated using the mask creation

544 tool in the Relion package (Scheres 2012). The final masked ectodomain map contained 32802
545 sub-volumes with a calculated resolution of 9.13 Å at 0.143 FSC cut-off value.
546
547 For asymmetric hVLP-Env map:
548 The initial sub-volumes used for generation of the asymmetric map were the same as that
549 used for the C3 symmetrized map described above. Refinement strategies were also nearly
550 identical between the two structures except the asymmetric map was generated with C1 symmetry.
551 However, the refinement and processing steps were carried out completely independent of each
552 other. The number of sub-volumes in the final C1 hVLP-Env structure was 29074 with a global
553 resolution of 10.67 Å at 0.143 FSC cut-off.
554
555 Structure of hVLP-Env and Gag layer from immature virions:
556 A total of 1520 sub-volumes from only immature virions were used to generate C3 and C1
557 symmetrized maps of membrane bound Env using 2Xbinned data in EMAN2 (Chen, Bell et al.
558 2019) by similar procedures as described above.
559 In the unmasked maps, a third density layer was observed underneath the membrane
560 bilayer. Relaxing symmetry of the C3-density map to C1, showed a more defined organization in
561 the Gag layer. Hence, a short, cylindrical mask enclosing only the Gag layer was used for local
562 refinement of the Gag layer using C1 symmetry, starting from the final refined positions derived
563 from the C3-symmetrized immature Env map. This focused refinement gave rise to a 23 Å map of
564 the Gag protein layer (0.143 FSC cut-off). The refined Gag-CA density map was fitted back into
565 the Gag-CA layer of the relaxed to C1 symmetry full Env map for further analyses.
566

567 Sub-tomogram averaged structure of BG505-Env from VLPs:

568 Purified BG505-VLPs were mixed with 10nm gold beads (Aurion BSA Gold Tracer 10nm)
569 at a ratio of 15:1 (v/v). The mixture was applied to C-Flat grids and plunge frozen using a Vitrobot
570 Mark IV (FEI Co.) similar to the procedure used for hVLPs above.

571 Frozen grids were imaged using a 300 kV Titan Krios with a Gatan K2 direct electron
572 detector and GIF energy filter with slit width of 20 eV. Tilt-series were collected in a dose-
573 symmetric tilting scheme from -54° to +54° with a step size of 3° using Leginon (Carragher,
574 Kisseberth et al. 2000) software. Tilt-series were collected in counting mode at a magnification of
575 53000X, corresponding to a pixel size of 2.58 Å per pixel. The total dose per tilt series was ~64-
576 68 $e^-/Å^2$. A total of 49 tilt-series were collected.

577 Tilt-series were imported into EMAN2's sub-tomogram averaging pipeline (Chen, Bell et
578 al. 2019). 1k X 1k tomograms were generated within EMAN2 using default parameters. Particle
579 points were picked manually in the e2spt_boxer.py interface (Chen, Bell et al. 2019). Further
580 refinement and processing steps were carried out similar to the hVLP-Env sub-tomogram
581 averaging procedures described above. Briefly, sub-volumes were initially extracted at 4xbinning
582 corresponding to a pixel size of 10.32 Å per pixel. Sub-tomogram refinement was carried using a
583 spherical mask including Env on surface and a part of the membrane. The initial model generated
584 for hVLP-Env in Relion (Scheres 2012, Bharat and Scheres 2016) was used as initial model for
585 BG505-Env also with low pass filtering to 60 Å. Sub-volumes were then re-extracted at 2X binning
586 using the particle orientations from the 4X binned refinement output. Sub-tomogram refinement
587 was repeated using the 2X binned data with a cylindrical mask covering only the ectodomain and
588 outer membrane layer. Particle orientations were locally refined, and duplicates were removed.
589 Sub-tilt refinement in EMAN2 was carried out using default parameters (Chen, Bell et al. 2019).

590 The final map contained 2773 sub-volumes with a calculated resolution of 16.7 Å at 0.143 FSC
591 cut-off value.
592
593 Model fitting and glycan modeling:
594 Full length Env structure from strain 92UG037.8 purified with detergents (PDB ID: 6ULC)
595 (Pan, Peng et al. 2020) was fitted as a rigid body into the 9.13 Å resolution hVLP-Env map. Each
596 protomer, comprising of gp120-gp41 heterodimer, was fitted individually into the map using
597 UCSF Chimera (Pettersen, Goddard et al. 2004). The unstructured loop region at the end of gp41,
598 comprising of amino acid residues 654-664, was fitted into the clearly delineated stalk density
599 using 'Flexible fitting' feature in Coot software (Emsley, Lohkamp et al. 2010). For modelling
600 glycan moieties, previously published high-resolution Env structures, PDB IDs: 5FUU and 5FYJ-
601 L, containing well-built glycan models were used as reference (Lee, Ozorowski et al. 2016,
602 Stewart-Jones, Soto et al. 2016). Appropriate glycan chains from these structures were copied into
603 corresponding glycan positions in the hVLP-Env map based on the presence of unoccupied
604 density. In regions where the unoccupied density was larger than the modeled glycan chains
605 available from the reference PDB structures, these extra densities were left un-modeled.
606 The final model of hVLP-Env, as generated above, was used for rigid body fitting into the
607 other sub-tomogram averaged maps of asymmetric hVLP-Env and immature hVLP-Env. All rigid
608 body fitting procedures were carried out using UCSF Chimera (Pettersen, Goddard et al. 2004).
609 Root mean square deviation (R.m.s.d) calculations between pairs of HIV Env structures
610 was carried out using UCSF Chimera (Pettersen, Goddard et al. 2004). Multiple sequence
611 alignments were carried out using the Clustal Omega web service (Madeira, Park et al. 2019).

612 Structure and tomographic images were generated using UCSF Chimera (Pettersen,
613 Goddard et al. 2004), ChimeraX (Pettersen, Goddard et al. 2021), IMOD's graphical user interface
614 (Kremer, Mastronarde et al. 1996) and ImageJ (Schneider, Rasband et al. 2012).
615
616 Neutralization assays:
617 ADA.CM.V4 hVLPs were prepared for neutralization assays as described above except omitting
618 the AT-2 inactivation step. Pseudotyped viruses were similarly produced by co-transfection of
619 HEK 293T cells using pSG3ΔEnv backbone plasmid and Env-complementation plasmid. Serial
620 dilutions of antibodies were added to virus and the mixture was incubated for 1 h at 37°C prior to
621 addition to TZM-bl target cells. DEAE-dextran was added to wells to a final concentration of 10
622 µg/ml. After incubating for 72 h at 37°C, cells were lysed, Bright-Glo luciferase reagent (Promega)
623 was added, and luminescence was measured using a Synergy H1 microplate reader (Bio-Tek).
624
625 Virus ELISA:
626 ELISAs on directly immobilized hVLPs were performed as previously described (Tong, Crooks
627 et al. 2012). Briefly ADA.CM.V4 hVLPs (prepared as detailed above and treated with or without
628 AT-2) were immobilized on microwell plates at a 20x concentration for 2 h at 37˚C. Plates were
629 blocked with 4% non-fat dry milk (NFDM) PBS for 1 h at 37˚C, probed with serial dilutions of
630 primary antibodies and, subsequently, goat anti-human-Fcɣ-HRP secondary antibody (Jackson) in
631 PBS + 0.4% NFDM, and with washes using PBS between each step (detergent was omitted from
632 all steps). Signal was developed using One-step Ultra TMB Substrate (ThermoFisher).
633

634 BG505.SOSIP expression and purification:

635 Soluble BG505.SOSIP protein was expressed and purified as previously described (Verkerke,
636 Williams et al. 2016). Expi293F cells grown in Freestyle 293 media (Thermo Scientific) were co-
637 transfected with plasmids containing the SOSIP sequence and furin protease in a 3:1 ratio using
638 PEI MAX (Polysciences). Six to seven days post-transfection the supernatant was cleared by
639 filtration and the SOSIP purified by *Galanthus nivalis* lectin affinity, followed by ion-exchange
640 and hydrophobic interaction chromatography. Trimeric product was buffer exchanged into PBS
641 and stored at 4°C.

642

643 Hydrogen-deuterium mass-spectroscopy (HDX-MS) of ADA.CM.V4 particles and
644 BG505.SOSIPs:

645 HDX-MS using quench lysis method:

646 Frozen stocks of ADA.CM.V4 VLP containing approximately 0.5mg/mL envelope protein or
647 purified BG505.SOSIP diluted to the same concentration were buffer-exchanged into HEPES-
648 buffered saline (HBS, 10mM HEPES-KOH, pH 7.4, 150mM NaCl) using Zeba Spin columns with
649 a 7kDa MWCO (Thermo Fisher). 10µL of VLP solution was diluted with 90µL of deuterated HBS
650 (Hepes Buffer Saline, pH 7.4) for the indicated labeling time. The reaction was quenched and lysed
651 by addition of an equal volume of 0.2% formic acid, 4M guanidine hydrochloride, 0.2M TCEP
652 (tris(2-carboxyethyl)phosphine), 0.2% DDM (n-Dodecyl-B-D-maltoside), followed by 30s
653 incubation on ice. 20µL of a 300mg/mL solution of ZrO_2 beads (HybridSPE-Phospholipid)
654 (Adhikary, Deredge et al. 2017) in 0.1% formic acid was then added to the solution, followed by
655 vortexing for 30seconds on ice. The bead/protein mixture was then moved to a 0.22µm cellulose
656 acetate centrifuge filter tube (Spin-X, Corning) and spun for 30s at 13,000xG, 0°C. The flow-

657 through was transferred to a thin-wall PCR tube and frozen in liquid nitrogen. Samples were
658 thawed on ice and passed over a custom packed pepsin column (2.1 × 50 mm) kept at 15°C with a
659 flow of 0.1% trifluoroacetic acid (TFA), 2% acetonitrile (ACN) at 200 µL/min for 5 minutes.

660 Digested peptides were collected on a Waters XSelect CSH C18 XP VanGuard Cartridge,
661 130Å, 2.5 µm, 2.1 mm X 5 mm before separation on a Waters ACQUITY UPLC Peptide CSH
662 C18 Column, 130Å, 1.7 µm, 1 mm X 100 mm using a gradient of 7 to 14% B over 1 minute, 14
663 to 30% B over 12.5 minutes, and 30 to 50% B over 1 minute, followed by washing with three rapid
664 gradients between 95 and 5% B (A: 0.1% formic acid, 0.025% trifluoroacetic acid, 2% acetonitrile;
665 B: 0.1% formic acid in 100% acetonitrile). The liquid chromatography system was coupled to a
666 Waters Synapt G2-Si Q-TOF with ion mobility enabled. Source and de-solvation temperatures
667 were 70°C and 130°C respectively. The StepWave ion guide settings were tuned to prevent non-
668 uniform gas phase proton exchange in the source (Guttman, Wales et al. 2016).

669 During the separation step, a series of 250 µL injections were used to clean the pepsin
670 column: (1) Fos-choline-12 (Anaspec) in 0.1% TFA; (2) 2 M GuHCl in 0.1% TFA; (3) 10% acetic
671 acid, 10% ACN and 5% IPA (Majumdar, Manikwar et al. 2012, Hamuro and Coales 2018). After
672 each gradient, the trap column was washed with a series of 250 µL injections: (1) 10% FA; (2)
673 30% trifluoroethanol; (3) 80% MeOH; (4) 66% 2-propanol, 34% ACN; (5) 80% ACN (Fang, Rand
674 et al. 2011).

675

676 <u>HDX-MS using solution digestion method:</u>

677 Env on hVLPs was quantified by SDS-PAGE using BG505 SOSIPs as a standard. HDX-MS
678 reactions were initiated by diluting 20 uL of either hVLPs or BG505 SOSIPs with 180 uL
679 deuteration buffer (10 mM Phosphate, 150 mM NaCl, 85% D_2O (Cambridge Isotope

680 Laboratories)) to a final pH = 7.45. Samples were deuterated for 5 seconds, 60 seconds, 30 minutes,
681 or 3 hours before being diluted 1:1 with ice cold quench buffer (8 M urea, 200 mM TCEP [tris(2-
682 carboxyethyl) phosphine] and 0.2% formic acid (FA)) to a final pH of 2.5. Quenched samples were
683 digested with 30 ug/mL of porcine pepsin (Worthington Labs) under quench conditions for 5
684 minutes on ice. Labeled peptides were purified by high speed centrifugation at 0°C (2 minutes at
685 25,000 rcf) and immediately flash frozen in liquid nitrogen. BG505 SOSIP samples were handled
686 identically to ensure consistent labeling and back exchange. Frozen samples were stored at -80°C
687 until analysis. All reactions were performed in duplicate.

688 Samples were thawed for 5 minutes on ice and manually injected into a custom built HDX
689 LC system kept at 0°C using a 500 uL sample loop. Samples were trapped on a Waters ACQUITY
690 UPLC CSH C18 VanGuard 130Å, 1.7 µm, 2.1 mm by 5 mm trap column for 7 minutes with a flow
691 of solvent A [2% acetonitrile, 0.1% FA, 0.025% trifluoroacetic acid (TFA)] at a rate of 150
692 µL/min. Peptides were resolved over a Waters ACQUITY UPLC CSH C18 130Å, 1.7 µm, 1 x 100
693 mm column using a 20 minute linear gradient of 3% to 50% solvent B (Solvent B: 100%
694 acetonitrile and 0.1% FA) and analyzed using Waters Synapt G2-Si Q-TOF as described above.
695 Following each injection, the sample loop and trap were washed as described above.

696 Deuterium uptake analysis was performed with HD-Examiner (Sierra Analytics) and HX-
697 Express v2 (10.1021/jasms.8b04435). For solution digestion experiments data was extracted using
698 CDCReader and analyzed using HXExpress V2 (Guttman, Weis et al. 2013) with binomial fitting
699 and bimodal deconvolution.

700 Internal exchange standards Pro-Pro-Pro-Ile [PPPI] and Pro-Pro-Pro-Phe [PPPF] were
701 included in each reaction to control for variations in ambient temperature during the labeling
702 reactions (10.1021/ac300535r). Back-exchange was measured by including bradykinin peptide at

703 2µg/mL in the deuterated buffer to serve as a fully deuterated control. The back-exchange level
704 ranged from 12-16% across experiments; deuterium uptake was not corrected.
705 Totally deuterated (TD) samples were prepared by collecting purified peptide eluent following
706 reverse phase LC separation of a pepsin digested undeuterated sample. Following evaporation of
707 the LC elution buffer the peptides were resuspended in HDX PBS pH 7.50 Buffer, deuterated in
708 deuteration Buffer for 1 hours at 65°C, and quenched and frozen as described above.
709 For peptide identification, un-deuterated peptides were collected from the LC system, dried
710 by speed-vac, and resuspended in 5% acetonitrie, 0.1% formic acid for re-injection on an Orbitrap
711 Fusion for MS/MS using EThcD fragmentation. Data was analyzed using Byonic (Protein Metrics)
712 and manually compared to undeuterated sample data.
713

714 Peptic digest analysis:

715 Peptic digest products were collected from the HDX chromatography system, dried by speed-
716 vaccuum, and resuspended in aqueous buffer for nanoscale liquid chromatography (nanoLC-MS)
717 using a 90-minute linear gradient from 2-40% acetonitrile. Products were analyzed on an Orbitrap
718 Fusion mass spectrometer (ThermoFisher Scientific) using a high-energy collisional dissociation
719 (HCD) product-dependent electron-transfer/high-energy collision dissociation (EThcD) method
720 with a targeted mass list method with a targeted mass list using HexNAc, HexHexNAc, and
721 Hex2HexNAc m/z (204, 366, and 528 respectively) to trigger EThcD.
722 Glycopeptide data were visualized and processed by Byonic™ (Version 3.8, Protein Metrics Inc.)
723 using a 10 ppm precursor and 10 ppm fragment mass tolerance. Glycopeptides were searched using
724 the N-glycan 309 mammalian database in Protein Metrics PMI-Suite and scored based on the

725 assignment of correct c- and z- fragment ions. The true-positive entities were further validated by
726 the presence of glycan oxonium ions m/z at 204 (HexNAc ions) and 366 (HexNAcHex ions).
727
728
729 **Supplemental Information:** Supplemental information can be found online at ***
730
731
732 **References:**

733 Adhikary, S., D. J. Deredge, A. Nagarajan, L. R. Forrest, P. L. Wintrode and S. K. Singh (2017).
734 "Conformational dynamics of a neurotransmitter:sodium symporter in a lipid bilayer." Proc Natl
735 Acad Sci U S A **114**(10): E1786-E1795.

736 Alfadhli, A., A. O. Staubus, P. R. Tedbury, M. Novikova, E. O. Freed and E. Barklis (2019).
737 "Analysis of HIV-1 Matrix-Envelope Cytoplasmic Tail Interactions." J Virol **93**(21).

738 Berndsen, Z. T., S. Chakraborty, X. Wang, C. A. Cottrell, J. L. Torres, J. K. Diedrich, C. A.
739 López, J. R. Yates, M. J. van Gils, J. C. Paulson, S. Gnanakaran and A. B. Ward (2020).
740 "Visualization of the HIV-1 Env glycan shield across scales." Proc Natl Acad Sci U S A
741 **117**(45): 28014-28025.

742 Bharat, T. A. and S. H. Scheres (2016). "Resolving macromolecular structures from electron
743 cryo-tomography data using subtomogram averaging in RELION." Nat Protoc **11**(11): 2054-
744 2065.

745 Cao, L., M. Pauthner, R. Andrabi, K. Rantalainen, Z. Berndsen, J. K. Diedrich, S. Menis, D. Sok,
746 R. Bastidas, S. R. Park, C. M. Delahunty, L. He, J. Guenaga, R. T. Wyatt, W. R. Schief, A. B.
747 Ward, J. R. Yates, D. R. Burton and J. C. Paulson (2018). "Differential processing of HIV
748 envelope glycans on the virus and soluble recombinant trimer." Nat Commun **9**(1): 3693.

749 Carragher, B., N. Kisseberth, D. Kriegman, R. A. Milligan, C. S. Potter, J. Pulokas and A.
750 Reilein (2000). "Leginon: an automated system for acquisition of images from vitreous ice
751 specimens." J Struct Biol **132**(1): 33-45.

752 Chakrabarti, B. K., L. M. Walker, J. F. Guenaga, A. Ghobbeh, P. Poignard, D. R. Burton and R.
753 T. Wyatt (2011). "Direct antibody access to the HIV-1 membrane-proximal external region
754 positively correlates with neutralization sensitivity." J Virol **85**(16): 8217-8226.

755 Checkley, M. A., B. G. Luttge and E. O. Freed (2011). "HIV-1 Envelope Glycoprotein
756 Biosynthesis, Trafficking, and Incorporation." J Mol Biol **410**(4): 582-608.

757 Chen, M., J. M. Bell, X. Shi, S. Y. Sun, Z. Wang and S. J. Ludtke (2019). "A complete data
758 processing workflow for cryo-ET and subtomogram averaging." Nat Methods **16**(11): 1161-
759 1168.

760 Emsley, P., B. Lohkamp, W. G. Scott and K. Cowtan (2010). "Features and development of
761 Coot." Acta Crystallogr D Biol Crystallogr **66**(Pt 4): 486-501.

762 Fang, J., K. D. Rand, P. J. Beuning and J. R. Engen (2011). "False EX1 signatures caused by
763 sample carryover during HX MS analyses." Int J Mass Spectrom **302**(1-3): 19-25.

764 Frank, G. A., K. Narayan, J. W. Bess, G. Q. Del Prete, X. Wu, A. Moran, L. M. Hartnell, L. A.
765 Earl, J. D. Lifson and S. Subramaniam (2015). "Maturation of the HIV-1 core by a non-
766 diffusional phase transition." Nat Commun **6**: 5854.

767 Frey, G., H. Peng, S. Rits-Volloch, M. Morelli, Y. Cheng and B. Chen (2008). "A fusion-
768 intermediate state of HIV-1 gp41 targeted by broadly neutralizing antibodies." Proc Natl Acad
769 Sci U S A **105**(10): 3739-3744.

770 Fu, Q., M. M. Shaik, Y. Cai, F. Ghantous, A. Piai, H. Peng, S. Rits-Volloch, Z. Liu, S. C.
771 Harrison, M. S. Seaman, B. Chen and J. J. Chou (2018). "Structure of the membrane proximal
772 external region of HIV-1 envelope glycoprotein." Proc Natl Acad Sci U S A **115**(38): E8892-
773 E8899.

774 Gray, E. S., M. C. Madiga, P. L. Moore, K. Mlisana, S. S. Abdool Karim, J. M. Binley, G. M.
775 Shaw, J. R. Mascola and L. Morris (2009). "Broad neutralization of human immunodeficiency
776 virus type 1 mediated by plasma antibodies against the gp41 membrane proximal external
777 region." J Virol **83**(21): 11265-11274.

778 Gui, L., J. L. Ebner, A. Mileant, J. A. Williams and K. K. Lee (2016). "Visualization and
779 Sequencing of Membrane Remodeling Leading to Influenza Virus Fusion." J Virol **90**(15): 6948-
780 6962.

781 Guttman, M., A. Cupo, J. P. Julien, R. W. Sanders, I. A. Wilson, J. P. Moore and K. K. Lee
782 (2015). "Antibody potency relates to the ability to recognize the closed, pre-fusion form of HIV
783 Env." Nat Commun **6**: 6144.

784 Guttman, M., N. K. Garcia, A. Cupo, T. Matsui, J. P. Julien, R. W. Sanders, I. A. Wilson, J. P.
785 Moore and K. K. Lee (2014). "CD4-induced activation in a soluble HIV-1 Env trimer." Structure
786 **22**(7): 974-984.

787 Guttman, M., M. Kahn, N. K. Garcia, S. L. Hu and K. K. Lee (2012). "Solution structure,
788 conformational dynamics, and CD4-induced activation in full-length, glycosylated, monomeric
789 HIV gp120." J Virol **86**(16): 8750-8764.

790 Guttman, M., T. E. Wales, D. Whittington, J. R. Engen, J. M. Brown and K. K. Lee (2016).
791 "Tuning a High Transmission Ion Guide to Prevent Gas-Phase Proton Exchange During H/D
792 Exchange MS Analysis." J Am Soc Mass Spectrom **27**(4): 662-668.

793 Guttman, M., D. D. Weis, J. R. Engen and K. K. Lee (2013). "Analysis of overlapped and noisy
794 hydrogen/deuterium exchange mass spectra." J Am Soc Mass Spectrom **24**(12): 1906-1912.

795 Hamuro, Y. and S. J. Coales (2018). "Optimization of Feasibility Stage for Hydrogen/Deuterium
796 Exchange Mass Spectrometry." J Am Soc Mass Spectrom **29**(3): 623-629.

797 Hill, C. P., D. Worthylake, D. P. Bancroft, A. M. Christensen and W. I. Sundquist (1996).
798 "Crystal structures of the trimeric human immunodeficiency virus type 1 matrix protein:
799 implications for membrane association and assembly." Proc Natl Acad Sci U S A **93**(7): 3099-
800 3104.

801 Huang, J., B. H. Kang, M. Pancera, J. H. Lee, T. Tong, Y. Feng, H. Imamichi, I. S. Georgiev, G.
802 Y. Chuang, A. Druz, N. A. Doria-Rose, L. Laub, K. Sliepen, M. J. van Gils, A. T. de la Peña, R.
803 Derking, P. J. Klasse, S. A. Migueles, R. T. Bailer, M. Alam, P. Pugach, B. F. Haynes, R. T.
804 Wyatt, R. W. Sanders, J. M. Binley, A. B. Ward, J. R. Mascola, P. D. Kwong and M. Connors
805 (2014). "Broad and potent HIV-1 neutralization by a human antibody that binds the gp41-gp120
806 interface." Nature **515**(7525): 138-142.

807 Ke, Z., J. Oton, K. Qu, M. Cortese, V. Zila, L. McKeane, T. Nakane, J. Zivanov, C. J. Neufeldt,
808 B. Cerikan, J. M. Lu, J. Peukes, X. Xiong, H. G. Kräusslich, S. H. W. Scheres, R. Bartenschlager
809 and J. A. G. Briggs (2020). "Structures and distributions of SARS-CoV-2 spike proteins on intact
810 virions." Nature **588**(7838): 498-502.

811 Kim, A. S., D. P. Leaman and M. B. Zwick (2014). "Antibody to gp41 MPER alters functional
812 properties of HIV-1 Env without complete neutralization." PLoS Pathog **10**(7): e1004271.

813 Kim, M., Z. Y. Sun, K. D. Rand, X. Shi, L. Song, Y. Cheng, A. F. Fahmy, S. Majumdar, G.
814 Ofek, Y. Yang, P. D. Kwong, J. H. Wang, J. R. Engen, G. Wagner and E. L. Reinherz (2011).
815 "Antibody mechanics on a membrane-bound HIV segment essential for GP41-targeted viral
816 neutralization." Nat Struct Mol Biol **18**(11): 1235-1243.

817 Kong, R., K. Xu, T. Zhou, P. Acharya, T. Lemmin, K. Liu, G. Ozorowski, C. Soto, J. D. Taft, R.
818 T. Bailer, E. M. Cale, L. Chen, C. W. Choi, G. Y. Chuang, N. A. Doria-Rose, A. Druz, I. S.
819 Georgiev, J. Gorman, J. Huang, M. G. Joyce, M. K. Louder, X. Ma, K. McKee, S. O'Dell, M.
820 Pancera, Y. Yang, S. C. Blanchard, W. Mothes, D. R. Burton, W. C. Koff, M. Connors, A. B.
821 Ward, P. D. Kwong and J. R. Mascola (2016). "Fusion peptide of HIV-1 as a site of vulnerability
822 to neutralizing antibody." Science **352**(6287): 828-833.

823 Kremer, J. R., D. N. Mastronarde and J. R. McIntosh (1996). "Computer visualization of three-
824 dimensional image data using IMOD." J Struct Biol **116**(1): 71-76.

825 Kwon, Y. D., M. Pancera, P. Acharya, I. S. Georgiev, E. T. Crooks, J. Gorman, M. G. Joyce, M.
826 Guttman, X. Ma, S. Narpala, C. Soto, D. S. Terry, Y. Yang, T. Zhou, G. Ahlsen, R. T. Bailer, M.
827 Chambers, G. Y. Chuang, N. A. Doria-Rose, A. Druz, M. A. Hallen, A. Harned, T. Kirys, M. K.
828 Louder, S. O'Dell, G. Ofek, K. Osawa, M. Prabhakaran, M. Sastry, G. B. Stewart-Jones, J.
829 Stuckey, P. V. Thomas, T. Tittley, C. Williams, B. Zhang, H. Zhao, Z. Zhou, B. R. Donald, L. K.
830 Lee, S. Zolla-Pazner, U. Baxa, A. Schon, E. Freire, L. Shapiro, K. K. Lee, J. Arthos, J. B.
831 Munro, S. C. Blanchard, W. Mothes, J. M. Binley, A. B. McDermott, J. R. Mascola and P. D.
832 Kwong (2015). "Crystal structure, conformational fixation and entry-related interactions of
833 mature ligand-free HIV-1 Env." Nat Struct Mol Biol **22**(7): 522-531.

834 Leaman, D. P. and M. B. Zwick (2013). "Increased functional stability and homogeneity of viral
835 envelope spikes through directed evolution." PLoS Pathog **9**(2): e1003184.

836 Lee, J. H., D. P. Leaman, A. S. Kim, A. Torrents de la Pena, K. Sliepen, A. Yasmeen, R.
837 Derking, A. Ramos, S. W. de Taeye, G. Ozorowski, F. Klein, D. R. Burton, M. C. Nussenzweig,
838 P. Poignard, J. P. Moore, P. J. Klasse, R. W. Sanders, M. B. Zwick, I. A. Wilson and A. B. Ward
839 (2015). "Antibodies to a conformational epitope on gp41 neutralize HIV-1 by destabilizing the
840 Env spike." Nat Commun **6**: 8167.

841 Lee, J. H., G. Ozorowski and A. B. Ward (2016). "Cryo-EM structure of a native, fully
842 glycosylated, cleaved HIV-1 envelope trimer." Science **351**(6277): 1043-1048.

843 Li, Z., W. Li, M. Lu, J. Bess, C. W. Chao, J. Gorman, D. S. Terry, B. Zhang, T. Zhou, S. C.
844 Blanchard, P. D. Kwong, J. D. Lifson, W. Mothes and J. Liu (2020). "Subnanometer structures
845 of HIV-1 envelope trimers on aldrithiol-2-inactivated virus particles." Nat Struct Mol Biol **27**(8):
846 726-734.

847 Madeira, F., Y. M. Park, J. Lee, N. Buso, T. Gur, N. Madhusoodanan, P. Basutkar, A. R. N.
848 Tivey, S. C. Potter, R. D. Finn and R. Lopez (2019). "The EMBL-EBI search and sequence
849 analysis tools APIs in 2019." Nucleic Acids Res **47**(W1): W636-W641.

850 Majumdar, R., P. Manikwar, J. M. Hickey, J. Arora, C. R. Middaugh, D. B. Volkin and D. D.
851 Weis (2012). "Minimizing carry-over in an online pepsin digestion system used for the H/D
852 exchange mass spectrometric analysis of an IgG1 monoclonal antibody." J Am Soc Mass
853 Spectrom **23**(12): 2140-2148.

854 Mastronarde, D. N. (2005). "Automated electron microscope tomography using robust prediction
855 of specimen movements." J Struct Biol **152**(1): 36-51.

856 Mastronarde, D. N. and S. R. Held (2017). "Automated tilt series alignment and tomographic
857 reconstruction in IMOD." J Struct Biol **197**(2): 102-113.

858 McGuire, A. T., S. Hoot, A. M. Dreyer, A. Lippy, A. Stuart, K. W. Cohen, J. Jardine, S. Menis,
859 J. F. Scheid, A. P. West, W. R. Schief and L. Stamatatos (2013). "Engineering HIV envelope
860 protein to activate germline B cell receptors of broadly neutralizing anti-CD4 binding site
861 antibodies." J Exp Med **210**(4): 655-663.

862 Nicastro, D., C. Schwartz, J. Pierson, R. Gaudette, M. E. Porter and J. R. McIntosh (2006). "The
863 molecular architecture of axonemes revealed by cryoelectron tomography." Science **313**(5789):
864 944-948.

865 Pan, J., H. Peng, B. Chen and S. C. Harrison (2020). "Cryo-EM Structure of Full-length HIV-1
866 Env Bound With the Fab of Antibody PG16." J Mol Biol **432**(4): 1158-1168.

867 Pandey, A. and A. P. Galvani (2019). "The global burden of HIV and prospects for control."
868 Lancet HIV **6**(12): e809-e811.

869 Pettersen, E. F., T. D. Goddard, C. C. Huang, G. S. Couch, D. M. Greenblatt, E. C. Meng and T.
870 E. Ferrin (2004). "UCSF Chimera--a visualization system for exploratory research and analysis."
871 J Comput Chem **25**(13): 1605-1612.

872 Pettersen, E. F., T. D. Goddard, C. C. Huang, E. C. Meng, G. S. Couch, T. I. Croll, J. H. Morris
873 and T. E. Ferrin (2021). "UCSF ChimeraX: Structure visualization for researchers, educators,
874 and developers." Protein Sci **30**(1): 70-82.

875 Piai, A., Q. Fu, Y. Cai, F. Ghantous, T. Xiao, M. M. Shaik, H. Peng, S. Rits-Volloch, W. Chen,
876 M. S. Seaman, B. Chen and J. J. Chou (2020). "Structural basis of transmembrane coupling of
877 the HIV-1 envelope glycoprotein." Nat Commun **11**(1): 2317.

878 Rantalainen, K., Z. T. Berndsen, A. Antanasijevic, T. Schiffner, X. Zhang, W. H. Lee, J. L.
879 Torres, L. Zhang, A. Irimia, J. Copps, K. H. Zhou, Y. D. Kwon, W. H. Law, C. A. Schramm, R.
880 Verardi, S. J. Krebs, P. D. Kwong, N. A. Doria-Rose, I. A. Wilson, M. B. Zwick, J. R. Yates, W.
881 R. Schief and A. B. Ward (2020). "HIV-1 Envelope and MPER Antibody Structures in Lipid
882 Assemblies." Cell Rep **31**(4): 107583.

883 Rawi, R., L. Rutten, Y. T. Lai, A. S. Olia, S. Blokland, J. Juraszek, C. H. Shen, Y. Tsybovsky, R.
884 Verardi, Y. Yang, B. Zhang, T. Zhou, G. Y. Chuang, P. D. Kwong and J. P. M. Langedijk
885 (2020). "Automated Design by Structure-Based Stabilization and Consensus Repair to Achieve
886 Prefusion-Closed Envelope Trimers in a Wide Variety of HIV Strains." Cell Rep **33**(8): 108432.

887 Rossio, J. L., M. T. Esser, K. Suryanarayana, D. K. Schneider, J. W. Bess, G. M. Vasquez, T. A.
888 Wiltrout, E. Chertova, M. K. Grimes, Q. Sattentau, L. O. Arthur, L. E. Henderson and J. D.
889 Lifson (1998). "Inactivation of human immunodeficiency virus type 1 infectivity with
890 preservation of conformational and functional integrity of virion surface proteins." J Virol
891 **72**(10): 7992-8001.

892 Roy, N. H., J. Chan, M. Lambelé and M. Thali (2013). "Clustering and mobility of HIV-1 Env at
893 viral assembly sites predict its propensity to induce cell-cell fusion." J Virol **87**(13): 7516-7525.

894 Scheres, S. H. (2012). "RELION: implementation of a Bayesian approach to cryo-EM structure
895 determination." J Struct Biol **180**(3): 519-530.

896 Schneider, C. A., W. S. Rasband and K. W. Eliceiri (2012). "NIH Image to ImageJ: 25 years of
897 image analysis." Nat Methods **9**(7): 671-675.

898 Schur, F. K., W. J. Hagen, M. Rumlová, T. Ruml, B. Müller, H. G. Kräusslich and J. A. Briggs
899 (2015). "Structure of the immature HIV-1 capsid in intact virus particles at 8.8 Å resolution."
900 Nature **517**(7535): 505-508.

901 Stadtmueller, B. M., M. D. Bridges, K. M. Dam, M. T. Lerch, K. E. Huey-Tubman, W. L.
902 Hubbell and P. J. Bjorkman (2018). "DEER Spectroscopy Measurements Reveal Multiple

903 Conformations of HIV-1 SOSIP Envelopes that Show Similarities with Envelopes on Native
904 Virions." Immunity **49**(2): 235-246.e234.

905 Stano, A., D. P. Leaman, A. S. Kim, L. Zhang, L. Autin, J. Ingale, S. K. Gift, J. Truong, R. T.
906 Wyatt, A. J. Olson and M. B. Zwick (2017). "Dense Array of Spikes on HIV-1 Virion Particles."
907 J Virol **91**(14).

908 Stewart-Jones, G. B., C. Soto, T. Lemmin, G. Y. Chuang, A. Druz, R. Kong, P. V. Thomas, K.
909 Wagh, T. Zhou, A. J. Behrens, T. Bylund, C. W. Choi, J. R. Davison, I. S. Georgiev, M. G.
910 Joyce, Y. D. Kwon, M. Pancera, J. Taft, Y. Yang, B. Zhang, S. S. Shivatare, V. S. Shivatare, C.
911 C. Lee, C. Y. Wu, C. A. Bewley, D. R. Burton, W. C. Koff, M. Connors, M. Crispin, U. Baxa, B.
912 T. Korber, C. H. Wong, J. R. Mascola and P. D. Kwong (2016). "Trimeric HIV-1-Env Structures
913 Define Glycan Shields from Clades A, B, and G." Cell **165**(4): 813-826.

914 Tedbury, P. R. and E. O. Freed (2014). "The role of matrix in HIV-1 envelope glycoprotein
915 incorporation." Trends Microbiol **22**(7): 372-378.

916 Tedbury, P. R., M. Novikova, S. D. Ablan and E. O. Freed (2016). "Biochemical evidence of a
917 role for matrix trimerization in HIV-1 envelope glycoprotein incorporation." Proc Natl Acad Sci
918 U S A **113**(2): E182-190.

919 Tong, T., E. T. Crooks, K. Osawa and J. M. Binley (2012). "HIV-1 virus-like particles bearing
920 pure env trimers expose neutralizing epitopes but occlude nonneutralizing epitopes." J Virol
921 **86**(7): 3574-3587.

922 van Gils, M. J. and R. W. Sanders (2013). "Broadly neutralizing antibodies against HIV-1:
923 templates for a vaccine." Virology **435**(1): 46-56.

924 Verkerke, H. P., J. A. Williams, M. Guttman, C. A. Simonich, Y. Liang, M. Filipavicius, S. L.
925 Hu, J. Overbaugh and K. K. Lee (2016). "Epitope-Independent Purification of Native-Like
926 Envelope Trimers from Diverse HIV-1 Isolates." J Virol **90**(20): 9471-9482.

927 Wang, Y., P. Kaur, Z. J. Sun, M. A. Elbahnasawy, Z. Hayati, Z. S. Qiao, N. N. Bui, C. Chile, M.
928 L. Nasr, G. Wagner, J. H. Wang, L. Song, E. L. Reinherz and M. Kim (2019). "Topological
929 analysis of the gp41 MPER on lipid bilayers relevant to the metastable HIV-1 envelope prefusion
930 state." Proc Natl Acad Sci U S A **116**(45): 22556-22566.

931 Ward, A. B. and I. A. Wilson (2015). "Insights into the trimeric HIV-1 envelope glycoprotein
932 structure." Trends Biochem Sci **40**(2): 101-107.

933 Wei, X., J. M. Decker, S. Wang, H. Hui, J. C. Kappes, X. Wu, J. F. Salazar-Gonzalez, M. G.
934 Salazar, J. M. Kilby, M. S. Saag, N. L. Komarova, M. A. Nowak, B. H. Hahn, P. D. Kwong and
935 G. M. Shaw (2003). "Antibody neutralization and escape by HIV-1." Nature **422**(6929): 307-
936 312.

937 Wyma, D. J., J. Jiang, J. Shi, J. Zhou, J. E. Lineberger, M. D. Miller and C. Aiken (2004).
938 "Coupling of human immunodeficiency virus type 1 fusion to virion maturation: a novel role of
939 the gp41 cytoplasmic tail." J Virol **78**(7): 3429-3435.

940 Xiong, Q., M. K. Morphew, C. L. Schwartz, A. H. Hoenger and D. N. Mastronarde (2009). "CTF
941 determination and correction for low dose tomographic tilt series." J Struct Biol **168**(3): 378-387.

942 Zheng, S. Q., E. Palovcak, J. P. Armache, K. A. Verba, Y. Cheng and D. A. Agard (2017).
943 "MotionCor2: anisotropic correction of beam-induced motion for improved cryo-electron
944 microscopy." Nat Methods **14**(4): 331-332.
945